Parametrization of CMS silicon detectors pulse shape and Form Factors determination

A. Buffini, S. Busoni, M. Meschini, G. Parrini

Università and INFN, Sezione di Firenze

Abstract

As far several experimental tests have exploited the performances of CMS silicon detectors front-end electronics. In this report available experimental results have been analysed in the framework of both a parametric than a circuit model, which have allowed predictions about expected noise and determination of circuit optimal working point.

1 Introduction

In CMS silicon detector signals are read by 128 channel VLSI circuits, each made by a preamplifier amd a shaper. During last two years physicists involved in silicon detectors setting-up have used a preliminar version (APV6 [1]) of the final electronics, whose analogic part is shown in figure 1.

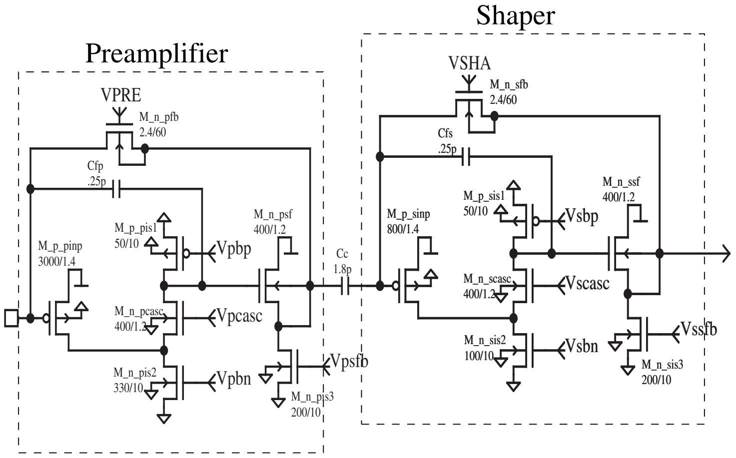

Figure 1: Analogic part of APV6 front-end electronics.

During tests several questions have arised about the criticity of some registers (VSHA, VPRE) which, settable via software, determine the pulse shape (figure 2) which is sampled and stored in the VLSI chip pipe line.

In this work we have concentrated on effects of VSHA register, which determines the shaper constant time, and on its influence on signal to noise ratio, by calculating form factors related to each profile.

In literature [1] APV6 output shape is referred as due to a two poles CR-RC filter, but this is a simple approximation only for a few VSHA values, as shown in figures 3.

During last months a run of a new VLSI chip version, called APV25 [2], has been realized. This chip is not yet available and it has not been tested on detectors; the knowledge of its performances is limited to some laboratory tests [4]. However we have applied the same models, used for APV6, to APV25 available data in literature [4].

2 APV6 output parametrization

In order to determine the transfer function of circuit shown in figure 1 two different ways can be followed. From one hand the transfer function can be determined analitically from the circuit scheme and the internal component values can be derived by trying to reobtain the measured experimental curves; this study has been faced in paragraph 4. On the other hand, different reasonable transfer functions $\tilde{F}(\omega)$ (Appendix) can be tried by fitting their inverse trasform F(t) to experimental data in their totality.

The function that best fits experimental points originates from a transfer function with four poles, two real and two complex; it is:

$$V(t) = QR \cdot \left[A \cdot e^{-\frac{t-t_0}{\tau_{1r}}} + B \cdot e^{-\frac{t-t_0}{\tau_{2r}}} + \left(C \cdot \sin\left(\omega_0(t-t_0)\right) + D \cdot \cos\left(\omega_0(t-t_0)\right)\right) \cdot e^{-\frac{t-t_0}{\tau_s}} \right] \quad (1)$$

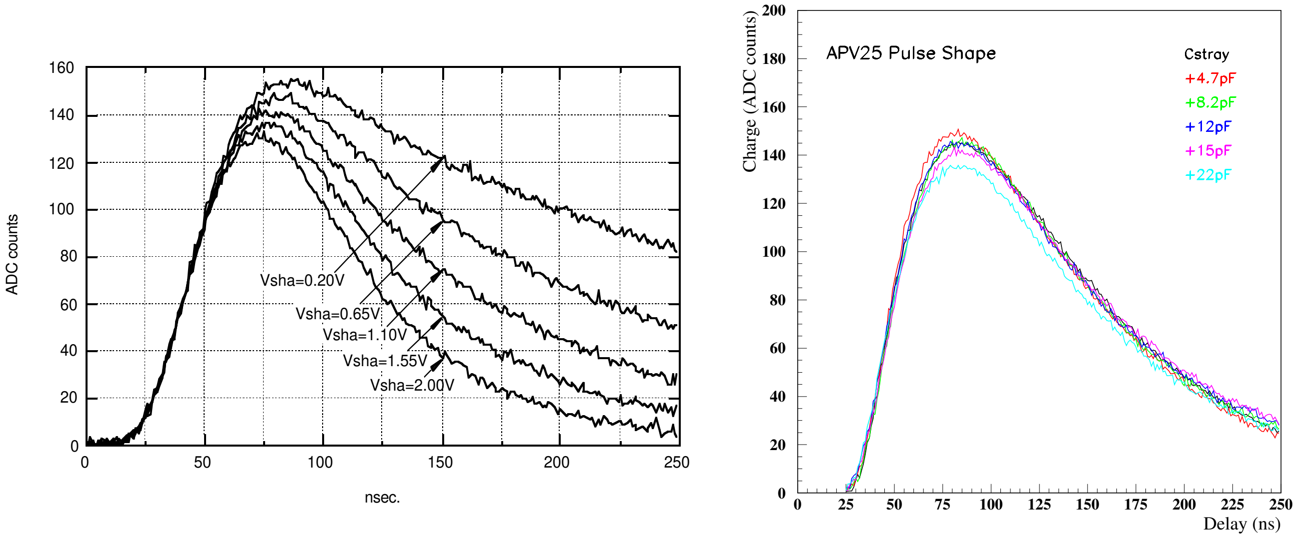

(a) (b)

Figure 2: (a) APV6 output for different VSHA values [3]; (b) APV25 output for different values of external capacitors [4]. VPRE is fixed.

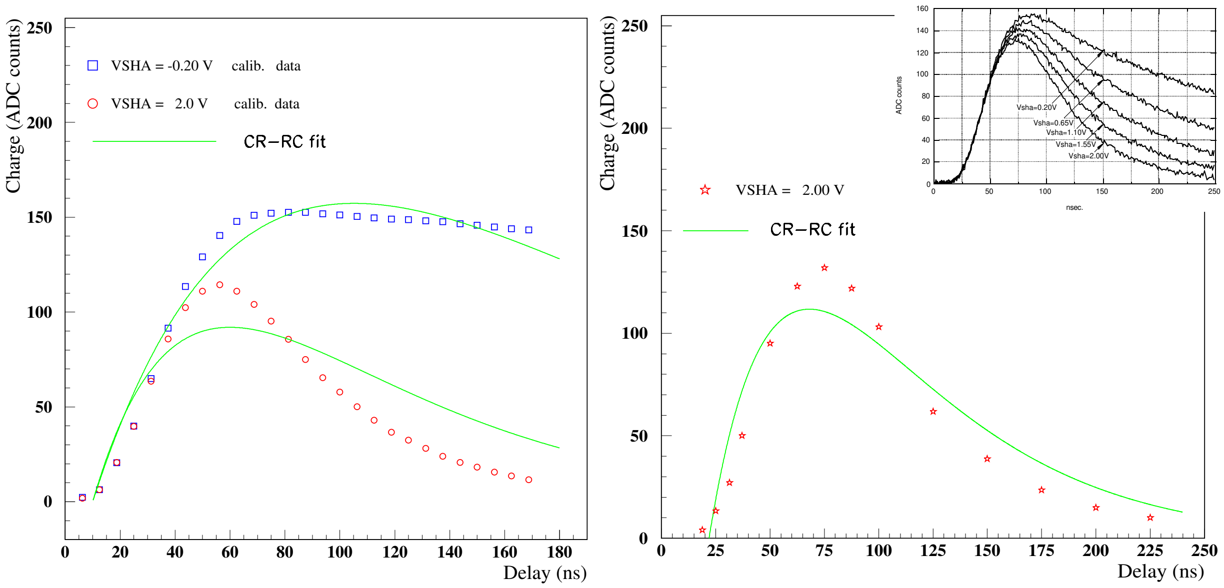

(a) (b)

Figure 3: CR-RC fit on APV6 output data taken from Ref. [5] (a) and on APV6 output data taken Ref. [3] (b). Used VSHA values are reported as well.

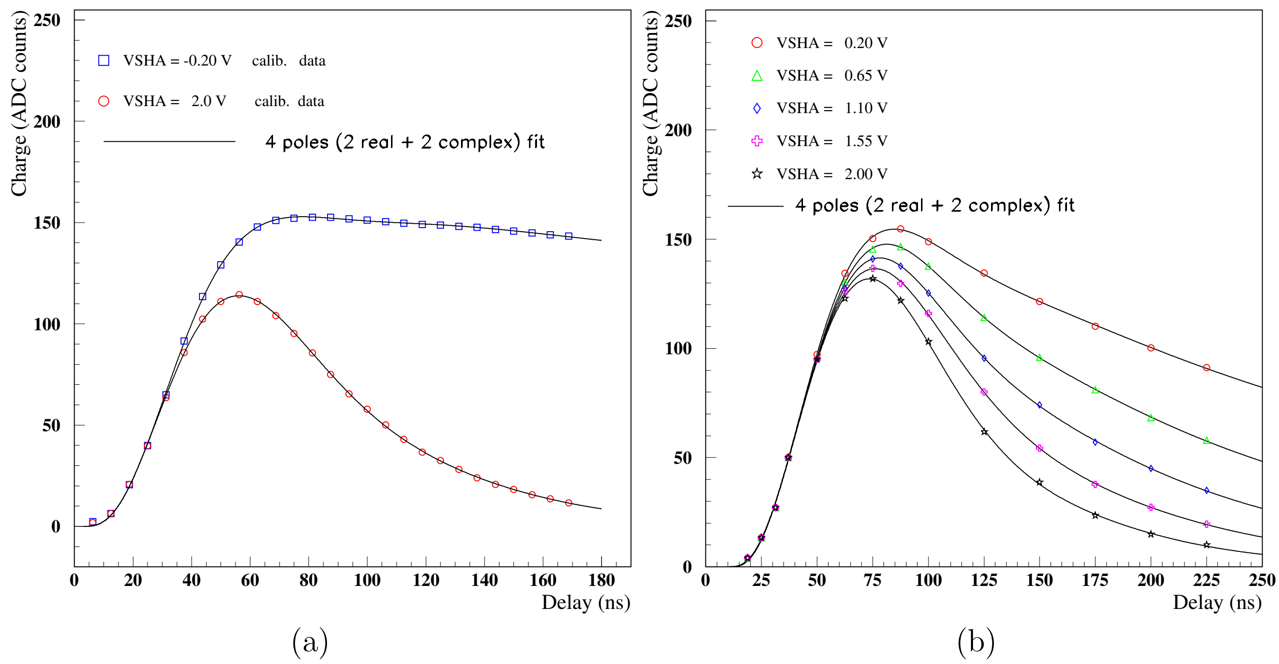

Figure 4: Fit of function (1) to Ref. [5] data (a), and to Ref. [3] data(b).

VSHA (V)	τ_{1r} (ns)	τ_{2r} (ns)	τ_s (ns)	$1/\omega_0$ (ns)	t_0 (ns)	QR
2.00	31.8 ± 1.2	31.8 ± 1.2	21.0 ± 0.6	14.9 ± 0.3	3.3 ± 0.3	9349
-0.20	23.4 ± 2.5	871.1 ± 155.2	21.8 ± 2.0	13.6 ± 0.4	2.9 ± 0.6	144760

Table 1: Results of function (1) free parameters to Ref. [5] data.

A, B, C, D depend on τ_{1r}, τ_{2r}, τ_s, ω_0 (Appendix), which toghether with the normalization factor QR and the signal arrival time t_0 are determined in the fit. Fit results are reported in figures 4 and in tables 1 and 2 for Ref. [5] and Ref. [3] data respectively.

From numerical results we see that three of the four poles are almost not sensitive to the VSHA register, which on the other hand seems to have a big influence on τ_{2r}. The VSHA register, which changes the value of the shaper feedback resistance R_{fsh}, is thus responsible of the pulse shape by moving one real pole of the transfer function.

In paragraph 4 we will see that QR is proportional to R_{fsh}. Figure 5 shows that τ_{2r} is proportional to QR so that it represents the shaper constant time.

The difference between pole values shown in table 1 and poles values in table 2 is easely explained as due to the use of two different VLSI chips.

VSHA (V)	τ_{1r} (ns)	τ_{2r} (ns)	τ_s (ns)	$1/\omega_0$ (ns)	t_0 (ns)	QR
2.00	25.7 ± 6.6	50.2 ± 5.7	28.1 ± 2.0	18.7 ± 1.2	10.4 ± 0.6	12643
1.55	18.5 ± 5.8	71.7 ± 4.3	25.6 ± 1.5	20.6 ± 2.4	10.9 ± 0.8	15625
1.10	23.6 ± 4.5	96.3 ± 5.1	26.7 ± 2.3	18.0 ± 1.1	10.3 ± 0.7	19962
0.65	23.0 ± 4.1	142.8 ± 7.0	26.3 ± 2.4	17.8 ± 1.1	10.3 ± 0.7	27761
0.20	22.2 ± 3.5	249.8 ± 12.8	24.8 ± 2.3	17.0 ± 1.0	10.7 ± 0.7	45775

Table 2: Results of function (1) free parameters to Ref. [3] data.

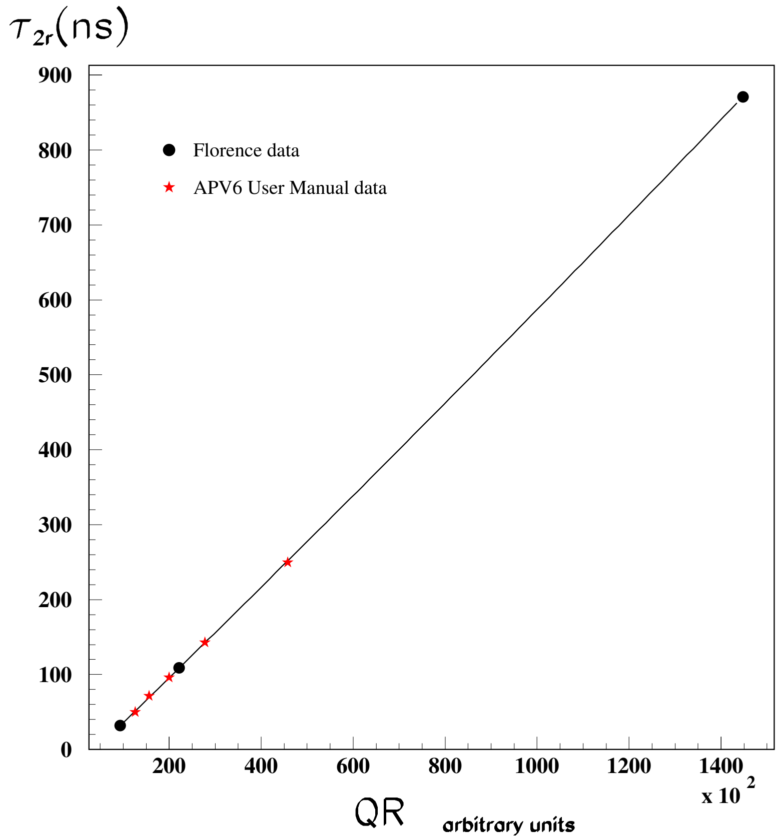

Figure 5: Linear dependence of τ_{2r} pole from amplitude QR.

3 Noise and Form Factors

Once the transfer function $\tilde{F}(\omega)$ of the box "preamplifier+shaper" (figure 6) is known, prediction on expected noise can be done.

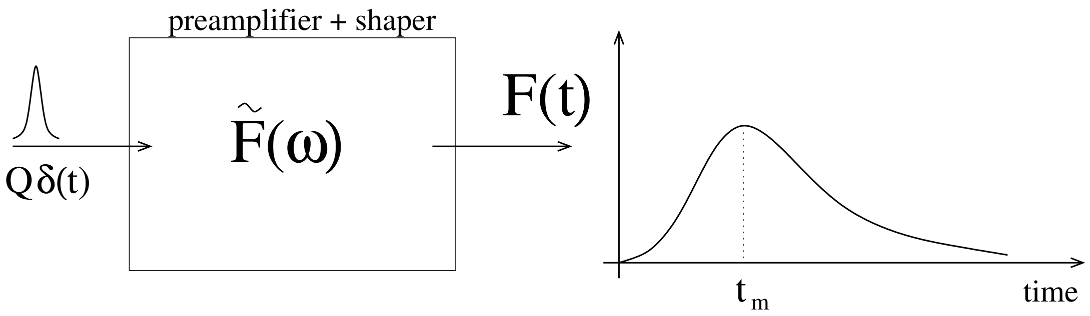

Figure 6: Scheme of preamplification and shaping of $Q\delta(t)$ signal particle. Measurement is performed on maximum at t_m.

Let $G(t)$ be the $F(t)/F(t_m)$ function and $\tilde{G}(\omega)$ its Fourier transform, then the input equivalent noise charge (ENC) can be written as:

$$\mathrm{ENC}_\mathrm{s}^2 = \frac{\mathrm{C}_\mathrm{tot}^2}{2\pi}\int_0^\infty e_n^2\omega^2|\tilde{G}(\omega)|^2\,d\omega$$
$$\mathrm{ENC}_\mathrm{p}^2 = \frac{1}{2\pi}\int_0^\infty i_n^2|\tilde{G}(\omega)|^2\,d\omega$$

where C_tot is the sum of detector capacitance with the input preamplifier capacitance and the feedback capacitance C_f (paragraph 4); e_n^2 e i_n^2 are the power spectra of the input equivalent noise sources.

e_n^2 is the series source, it originates mainly from the preamplifier input transistor and can be written as:

$$e_n^2 \simeq 2.7 \cdot \frac{KT}{G} + \frac{F}{WL}\cdot\frac{1}{f^\alpha}$$

where K is the Boltzman constant, T the temperature, G the cascode input transistor transonductance. In the second term, f is the frequency, F and α are empiric parameters, while W and L are the input transistor channel width and lenght.

i_n^2 is the parallel source, due mainly to detector polarization current (I_s) and polarization resistance R_p. Its expression is:

$$i_n^2 = \frac{4KT}{R_p} + 2qI_s$$

The series power spectrum has a white component and a $1/f^\alpha$ one, called "flicker" noise, while parallel power spectrum is just white.

For $\alpha = 1$:

VSHA (V)	t_m (ns)	$\mathrm{K^{ser}}$	$\frac{\mathrm{K^{ser}}}{\mathrm{t_m}}$ ($\mathrm{ns^{-1}}$)	$\mathrm{K^{par}}$	$\mathrm{K^{par} \cdot t_m}$ (ns)	$\mathrm{R}_{1/f}$
-0.20	75.1	1.475	$1.96{\cdot}10^{-2}$	6.69	502.78	4.33
0.56	62.0	1.611	$2.60{\cdot}10^{-2}$	1.53	94.99	3.26
2.00	52.8	1.825	$3.46{\cdot}10^{-2}$	1.02	53.96	3.18

Table 3: Form factors and flicker noise for sampled signal (1) derived from Ref. [5] data.

VSHA (V)	t_m (ns)	$\mathrm{K^{ser}}$	$\frac{\mathrm{K^{ser}}}{\mathrm{t_m}}$ ($\mathrm{ns^{-1}}$)	$\mathrm{K^{par}}$	$\mathrm{K^{par} \cdot t_m}$ (ns)	$\mathrm{R}_{1/f}$
0.20	73.9	1.514	$2.05{\cdot}10^{-2}$	2.20	162.49	3.38
0.65	71.0	1.588	$2.24{\cdot}10^{-2}$	1.52	108.04	3.19
1.10	67.8	1.677	$2.47{\cdot}10^{-2}$	1.25	84.60	3.13
1.55	65.2	1.761	$2.70{\cdot}10^{-2}$	1.10	71.57	3.15
2.00	63.2	1.853	$2.93{\cdot}10^{-2}$	0.98	62.17	3.15

Table 4: Form factors and flicker noise for sampled signal (1) derived from Ref. [3] data.

$$\begin{aligned}
\mathrm{ENC_s^2} &= C_{\mathrm{tot}}^2 \cdot [\, 2KTR_s \cdot \overbrace{\int_0^\infty \left|\frac{dG(t)}{dt}\right|^2 dt}^{\mathrm{K^{ser}/t_m}} + \frac{F}{WL} \cdot \overbrace{\int_0^\infty \omega |\tilde{G}(\omega)|^2 \, d\omega}^{\mathrm{R_{1/f}}} \,] \\
\mathrm{ENC_p^2} &= \frac{1}{2}\left(\frac{4KT}{R_p} + 2qI_s\right) \cdot \underbrace{\int_0^\infty |G(t)|^2 \, dt}_{\mathrm{K^{par} \cdot t_m}}
\end{aligned}$$

where $\mathrm{K^{ser}}$ and $\mathrm{K^{par}}$ are dimensionless constants, called form factors, which depend just from the output pulse shape.

For a two coincident poles shaper (semigaussian) the form factors are:

$$\mathrm{K^{ser}} = \mathrm{K^{par}} = \frac{e^2}{4} = 1.84726\ldots$$

Moreover, for a semigaussian shaper the dimensionless flicker term $\mathrm{R}_{1/f}$ does not depend, for $\alpha = 1$, on sampling time t_m and results $\mathrm{R}_{1/f} = e^2/2$.

As comparison with semigaussian form factors, usually used to foresee expected noise, we have determined form factors for the four poles transfer function (A-14). Results obtained both for Ref. [5] and Ref. [3] data are shown in tables 3 and 4.

In the ideal situation where τ_{1r}, τ_s and ω_0 do not depend at all from VSHA, samplig time t_m is a function just of τ_{2r}, so that we can predict the behaviour of serial, parallel and flicker noise versus sampling time, by varying τ_{2r}, that is the VSHA register.

Using values reported in tables 1 and 2, and fixing the three less sensible poles to VSHA to their mean values, we have obtained results shown in figures 7 and 8.

Results in figure 7 are obtained by using the values: $\tau_{1r} = 30.0 \pm 2.0$ ns, $\tau_s = 21.5 \pm 1.0$ ns, $1/\omega_0 = 14.5 \pm 0.5$ ns, and by varying τ_{2r} from 10 ns to 300 ns. In order to estimate the effect of the three pole variation, we calculated, for each τ_{2r} value, 500 points by varying, according to normal statistics, τ_{1r}, τ_s and $1/\omega_0$ around their mean values. Such points have then been superposed to the curves computed for mean values.

Results in figure 8 are obtained for values: $\tau_{1r} = 23.0 \pm 3.0$ ns, $\tau_s = 26.5 \pm 2.0$ ns, $1/\omega_0 = 19.0 \pm 2.0$ ns, by varying τ_{2r} from 10 ns to 260 ns.

In all cases we can see that in the range of used VSHA values the expected noise for actual APV6 pulse shape is lower than for semigaussian shaper.

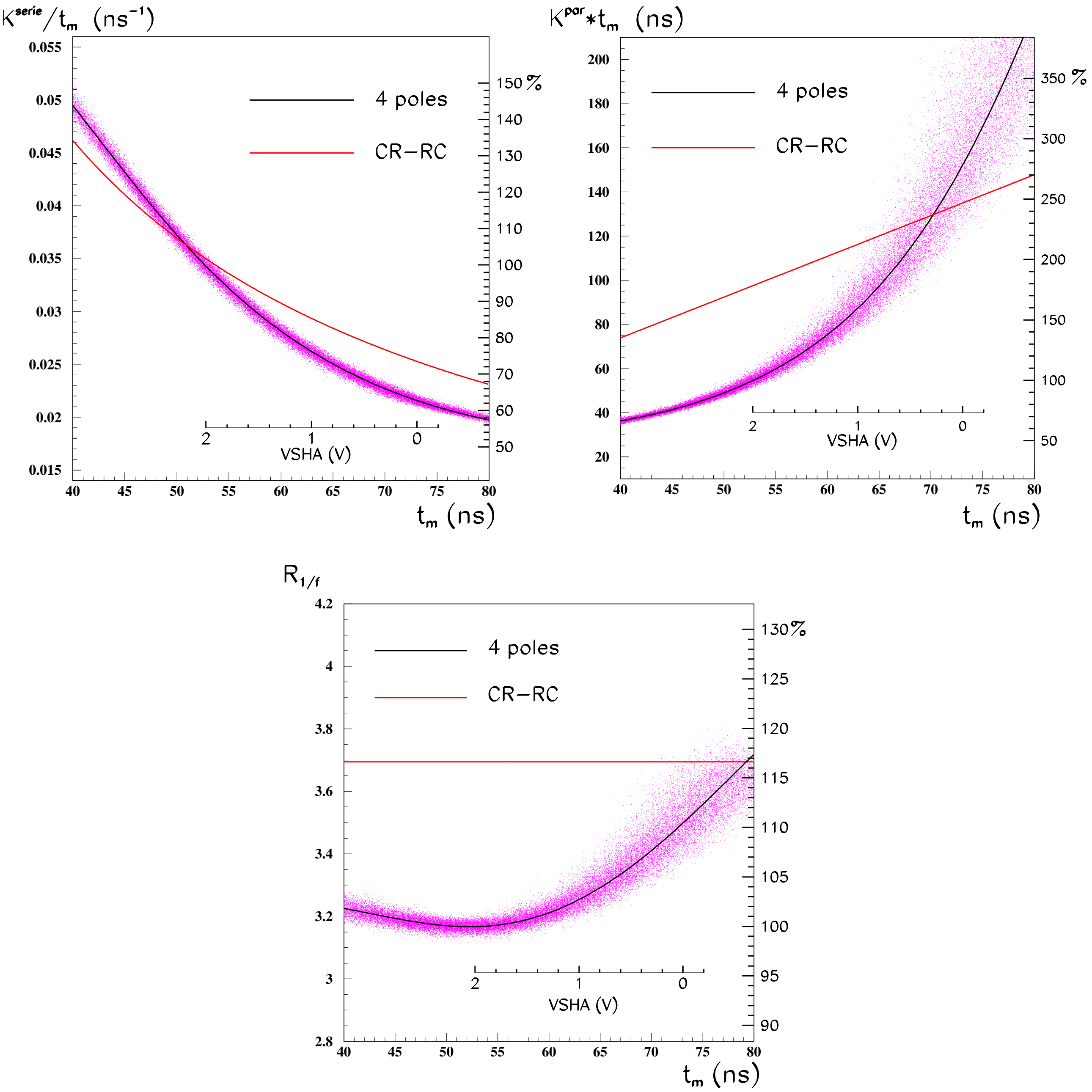

Figure 7: Series, parallel and flicker noise versus sampling time of the four pole function derived from Ref. [5] data. Right scale gives the ratio with VSHA=2.0V value. VSHA (V) scale gives t_m values used in the experimentation. Points around the solid curve give an estimation of variation effect of the three poles fixed in the noise procedure calculation.

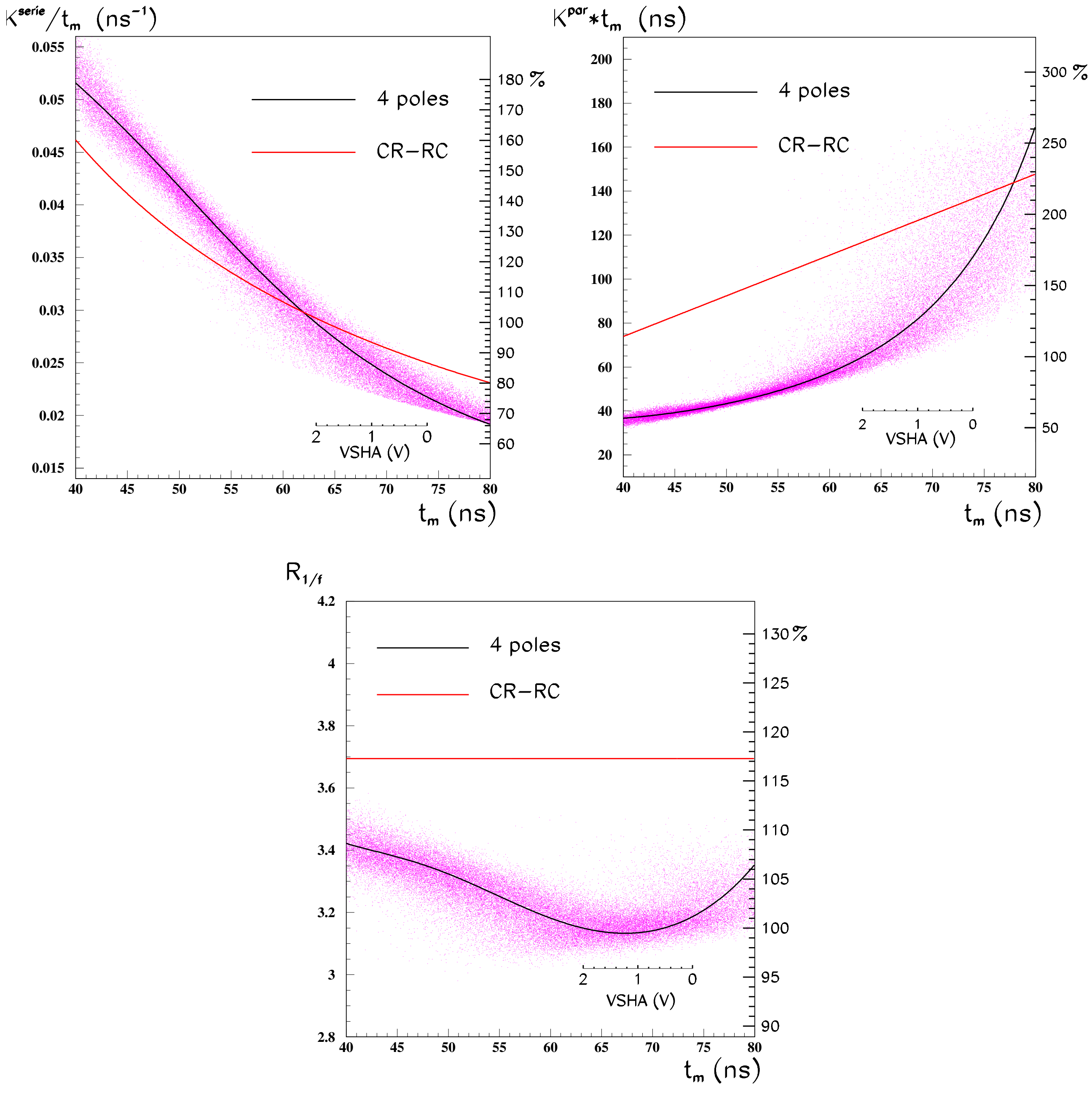

Figure 8: Series, parallel and flicker noise versus sampling time of the four pole function derived from Ref. [3] data. Right scale gives the ratio with VSHA=2.0V value. VSHA (V) scale gives t_m values used in the experimentation. Points around the solid curve give an estimation of variation effect of the three poles fixed in the noise procedure calculation.

4 Circuit analysis of APV6 single readout channel

In figure 9(a) the equivalent circuit of one of 128 APV6 readout channels is shown; both preamplifier than shaper part are based on a cascode (shaded rectangular) with a $C_f = 0.25$ pF feedback; the cascode output, after a source follower, is again fed-back through the feedback transistor channel, whose value can be changed by varying VPRE and VSHA voltage.

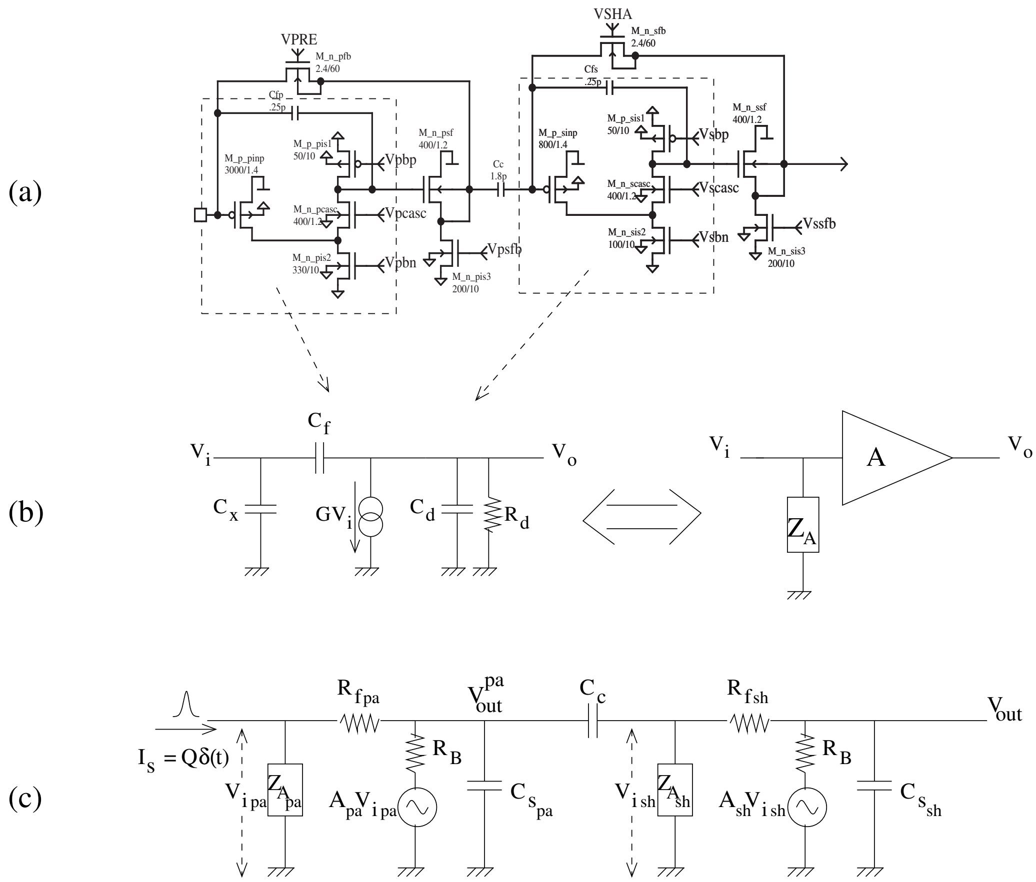

Figure 9: Equivalent scheme of APV6 circuit.

In order to calculate APV6 transfer function and input impedance, we have isolated the cascode with feedback (figure 9(b)). C_x is the input gate capacitance of first transistor, plus, in case of preamplifier, an external capacitance due to the detector; G is the input transistor transconductance while C_d and R_d are respectively the drain capacity and resistance of cascode output transistor.

The circuit is schematized as an ideal amplifier A with input impedance Z_A, whose expressions are:

$$A = \left(-G + \frac{1}{Z_f}\right) \cdot \frac{Z_d Z_f}{Z_d + Z_f}$$

$$Z_A = \frac{Z_x \cdot (Z_f + Z_d)}{Z_f + Z_d + Z_x + G Z_x Z_d}$$

with $Z_x = \frac{1}{j\omega C_x}$, $Z_f = \frac{1}{j\omega C_f}$, $Z_d = \frac{R_d}{1+j\omega C_d R_d}$.

The overall scheme is shown in figure 9(c) where voltage generators with serial resistance R_B represent the cascode with the source follower in output. R_B is the follower output resistance, R_{fpa} and R_{fsh} are the feedback resistances drived by VPRE and VSHA registers, and C_{Spa} and C_{Ssh} are capacitances at preamplifier and shaper output.

Using the above schematizations, the calculation of transfer function $F(\omega)$ can be performed analitically:

$$
\begin{aligned}
Z_c &= \frac{1}{j\omega C_c} \\
Z_{Lsh} &= \frac{1}{j\omega C_{Ssh}} \\
Z_{INsh} &= Z_c + \frac{Z_{Ash}}{Z_{Ash} + R_{fsh}} \cdot \left(R_{fsh} + \frac{Z_{Ash} Z_{Lsh}(R_B + A_{sh} R_{fsh})}{(R_{fsh} + Z_{Ash})(R_B + Z_{Lsh}) + Z_{Lsh}(R_B - A_{sh} Z_{Ash})} \right) \\
Z_{Lpa} &= Z_{INsh} // C_{Spa} = \frac{Z_{INsh}}{1 + j\omega Z_{INsh} C_{Spa}} \\
T_{pa} &= \frac{\mathcal{V}^{pa}_{\text{out}}}{I_s} = \frac{Z_{Apa} Z_{Lpa}(R_B + A_{pa} R_{fpa})}{(R_{fpa} + Z_{Apa})(R_B + Z_{Lpa}) + Z_{Lpa}(R_B - A_{pa} Z_{Apa})}
\end{aligned}
$$

$$
\begin{aligned}
F(\omega) &= \frac{\mathcal{V}_{\text{out}}}{I_s} \qquad (2) \\
&= \frac{Z_{Ash} Z_{Lsh}(R_B + A_{sh} R_{fsh})(R_{fsh} + Z_{Ash}) \cdot T^2_{pa}}{Z_{Apa} Z_{Lpa}(Z_c Z_{Ash} + Z_c R_{fsh} + Z_{Ash} R_{fsh})(R_B + A_{pa} R_{fpa}) + Z^2_{Ash} Z_{Lsh}(R_B + A_{sh} R_{fsh}) T_{pa}} \\
&\simeq R_{fsh} \cdot \frac{j\omega R_{fpa} C_c \cdot (1 - j\omega\tau_0)}{1 + j\omega a - \omega^2 b - j\omega^3 c + \omega^4 d + j\omega^5 e + \omega^6 f}
\end{aligned}
$$

The transfer function $F(\omega)$ has an amplitude which is proportional to R_{fsh} and shows six poles and two zeroes[1], which after a double pole zero cancellation, even if approximative, is compatible with results derived from four pole function fit.

Circuit free parameters can hence be determined by making the inverse transform of (2) and by comparing it with experimental points shown in figures 2(a) and 3(a). This procedure has been automatized by using the C06LBF function of NAG library, for inverse transform computation, and MINUIT [6] program for fit.

We has thus found a set of values for circuit parameters, reported in tables 5 and 6, relatives to curves in figure 10.

An advantage coming from this analysis is a greater physical understanding of circuit which allows interesting estimations when electronic read-out circuit is plugged to a detector.

[1] τ_0, a, b, c, d, e, f are function of circuit parameters.

C_d	=	0.33 pF		R_{dsh}	=	74.8 KΩ
C_{Ssh}	=	2.64 pF		R_{dpa}	=	37.0 KΩ
C_{Spa}	=	4.30 pF		R_{fpa}	=	27139 KΩ
C_{xsh}	=	3.76 pF		R_B	=	3.1 KΩ
C_{xpa}	=	23.6 pF		G_{pa}	=	$\frac{1}{349\Omega}$
C_p	=	0.27 pF		G_{sh}	=	$\frac{G_{pa}}{5.8}$
R_{fsh}	=	2645.5 KΩ	per	VSHA	=	-0.2 V
R_{fsh}	=	91.4 KΩ	per	VSHA	=	2.0 V

Table 5: Fit results for circuit parameters to Ref. [5] data.

C_d	=	0.13 pF		R_{dsh}	=	210.0 KΩ
C_{Ssh}	=	4.28 pF		R_{dpa}	=	113.0 KΩ
C_{Spa}	=	2.38 pF		R_{fpa}	=	22935 KΩ
C_{xsh}	=	7.91 pF		R_B	=	4.1 KΩ
C_{xpa}	=	33.5 pF		G_{pa}	=	$\frac{1}{305\Omega}$
C_p	=	0.20 pF		G_{sh}	=	$\frac{G_{pa}}{4.1}$
R_{fsh}	=	573.6 KΩ	per	VSHA	=	0.20 V
R_{fsh}	=	339.3 KΩ	per	VSHA	=	0.65 V
R_{fsh}	=	240.4 KΩ	per	VSHA	=	1.10 V
R_{fsh}	=	186.3 KΩ	per	VSHA	=	1.55 V
R_{fsh}	=	150.3 KΩ	per	VSHA	=	2.00 V

Table 6: Fit results for circuit parameters to Ref. [3] data.

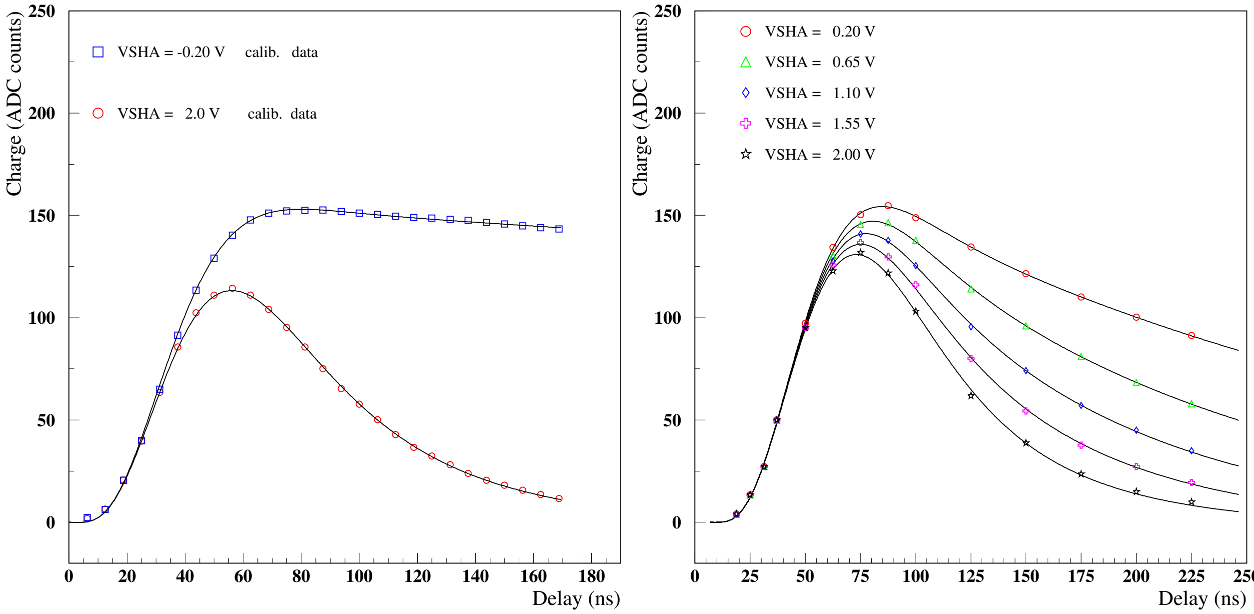

Figure 10: Fit of circuit free parameters to experimental data of Ref. [5] (a) and of Ref. [3] (b).

An interesting information, which is not experimentally available, but that can now be derived, regards APV6 input impedance, whose analitical expression is:

$$Z_{IN} = \frac{Z_{Apa} \cdot (R_{fpa} + T_{pa})}{Z_{Apa} + R_{fpa}} \quad (3)$$

Using values in tables 5 and 6, we found input impedances reported in figure 11. Such impedances are not sensitive to VSHA value; at low frequencies (f < 100 KHz) they show a low pass filter behavior:

$$Z_{IN} = \frac{R^M_{fpa}}{1 + j\omega R^M_{fpa}(C_{xpa} + C^M_f)}$$

where R^M_{fpa} and C^M_f are the preamplifier feedback Miller resistance and capacitance:

$$\begin{cases} R^M_{fpa} = \frac{R_{fpa}}{1+G_{pa}R_{dpa}} \\ C^M_f = C_f \cdot (1 + G_{pa}R_{dpa}) \end{cases}$$

At higher frequencies (f > 50 MHz) impedances show a slope of -20db/dec, characteristic of a capacitor ($\varphi \simeq -\pi/2$), whose value C_y results:

$$C_y = C_{xpa} + \frac{C_f \cdot C_d}{C_f + C_d}$$

Another interesting information is the inverse trasform of input impedance (figure 12(a)). It gives the time shape of preamplifier input signal since APV6 input sees a voltage:

$$\mathrm{V_{IN}}(\mathrm{t}) = Q_s \cdot Z_{IN}(t)$$

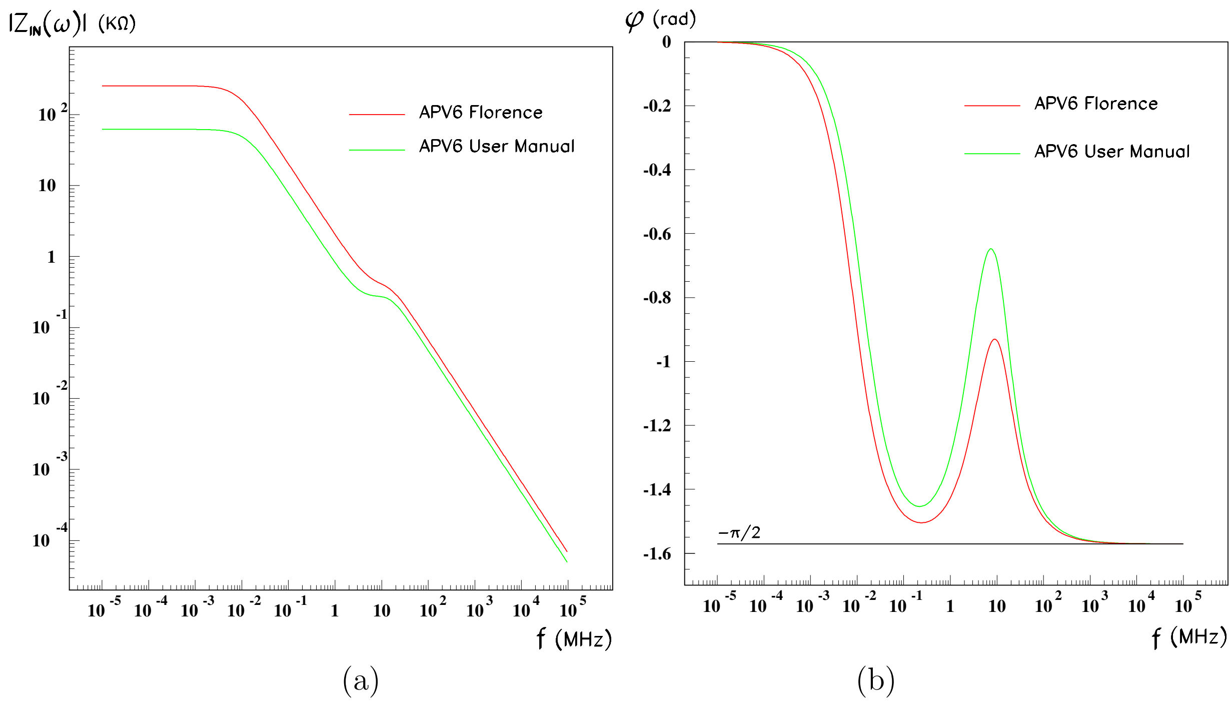

Figure 11: Module (a) and phase (b) of APV6 input impedance.

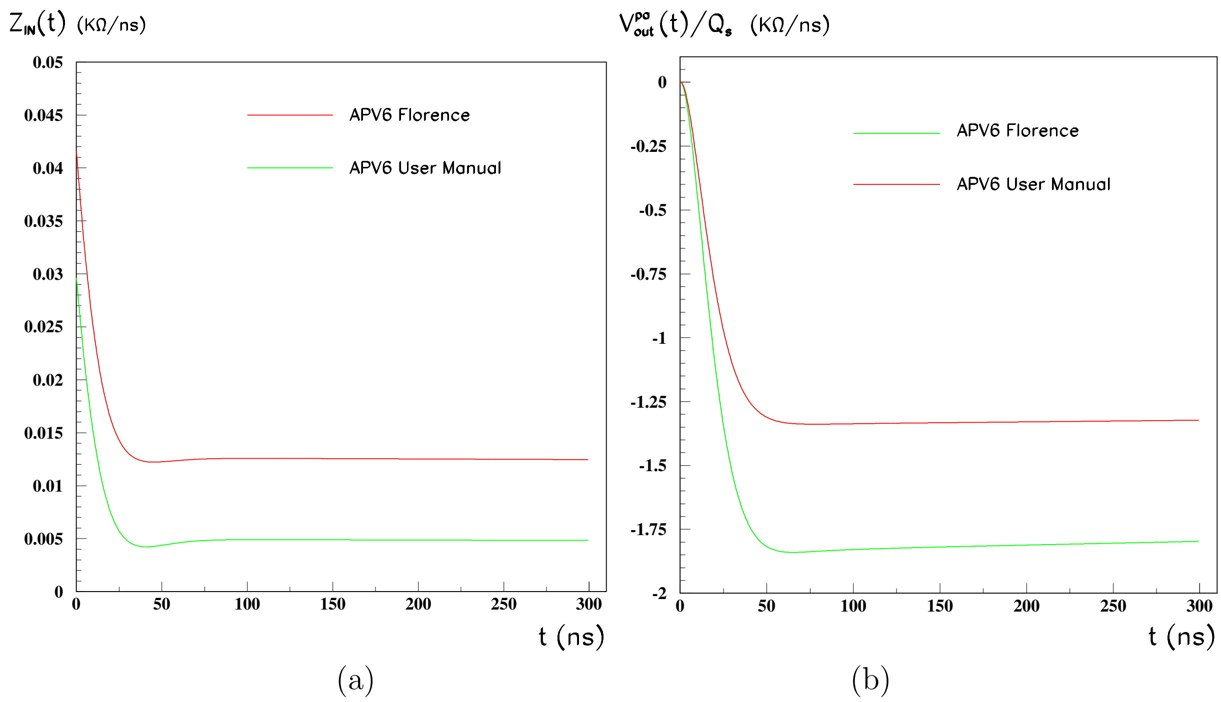

Figure 12: Inverse Fourier transform of input impedance (a) and preamplifier output (b) for APV6.

5 A first look at APV25

A similar study to what done for APV6 has been performed for APV25 by using experimental points shown in figure 2(b) for two different values of external capacitors.

Using a transfer function with three real poles, two of them coincident, we found a good agreement of fit with experimental point, as shown in figure 13.

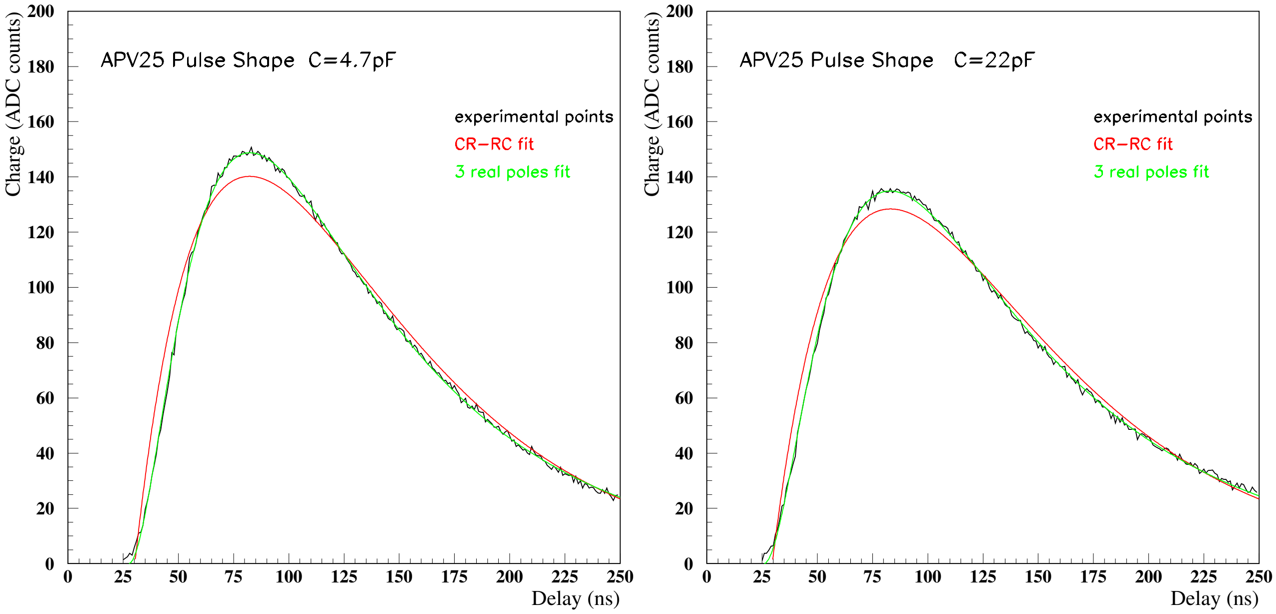

Figure 13: Fit of a three real pole transfer funcion and a semigaussian function to APV25 data.

The function used in the fit (A-8) is:

$$V(t) = QR \cdot \frac{\tau_1}{(\tau_1 - \tau_2)^2} \cdot \left[e^{-\frac{t-t_0}{\tau_1}} - \left(1 + \frac{\tau_1 - \tau_2}{\tau_1 \tau_2} \cdot (t - t_0) \right) \cdot e^{-\frac{t-t_0}{\tau_2}} \right]$$

Table 7 reports fit numerical results.

C_{ext} (pF)	τ_1 (ns)	τ_2 (ns)	t_0 (ns)	QR
4.7	78.0	16.9	25.5	19927
22	82.8	17.4	25.8	19005

Table 7: Fit results for free parameters of three pole function to APV25 data.

Since preamplifier and shaper circuit scheme of APV25 single channel is similar to APV6 one, but from some declared variations [2] as $C_f = 0.15$ pF and $C_c = 1.4$ pF, transfer function and input impedance can be computed in similar way to what done in paragraph 4. By fitting the transfer function (2) to experimental data shown in figure 2(b) for two different external capacitors we found for circuit parameters the values reported in table 8, which give the pulse shape in figure 14.

Fitted values, as in previous paragraph, allow calculation of input impedance (figure 15) and input signal (figure 16(a)).

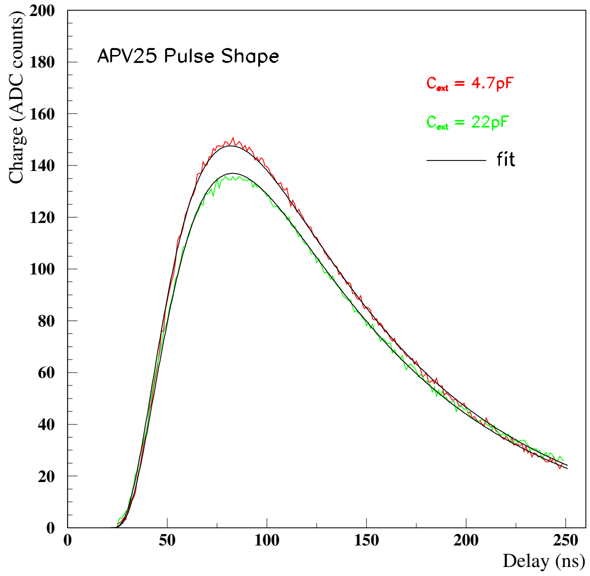

Figure 14: Fit of circuit parameters to APV25 data.

C_d	$=$	0.11 pF	R_{dsh}	$=$	28.3 KΩ
C_{Ssh}	$=$	2.8 pF	R_{dpa}	$=$	48.7 KΩ
C_{Spa}	$=$	2.4 pF	R_{fsh}	$=$	249.2 KΩ
C_{xsh}	$=$	8.3 pF	R_{fpa}	$=$	27256 KΩ
C_{xpa}	$=$	$23.4^{+4.7}_{+22}$ pF	R_B	$=$	4.4 KΩ
G_{pa}	$=$	$\frac{1}{37.2\Omega}$	G_{sh}	$=$	$\frac{G_{pa}}{21.7}$

Table 8: Numerical fit results of circuit parameters to APV25 data. The two different external capacitors C_{xpa}, relative to the two curves, are reported.

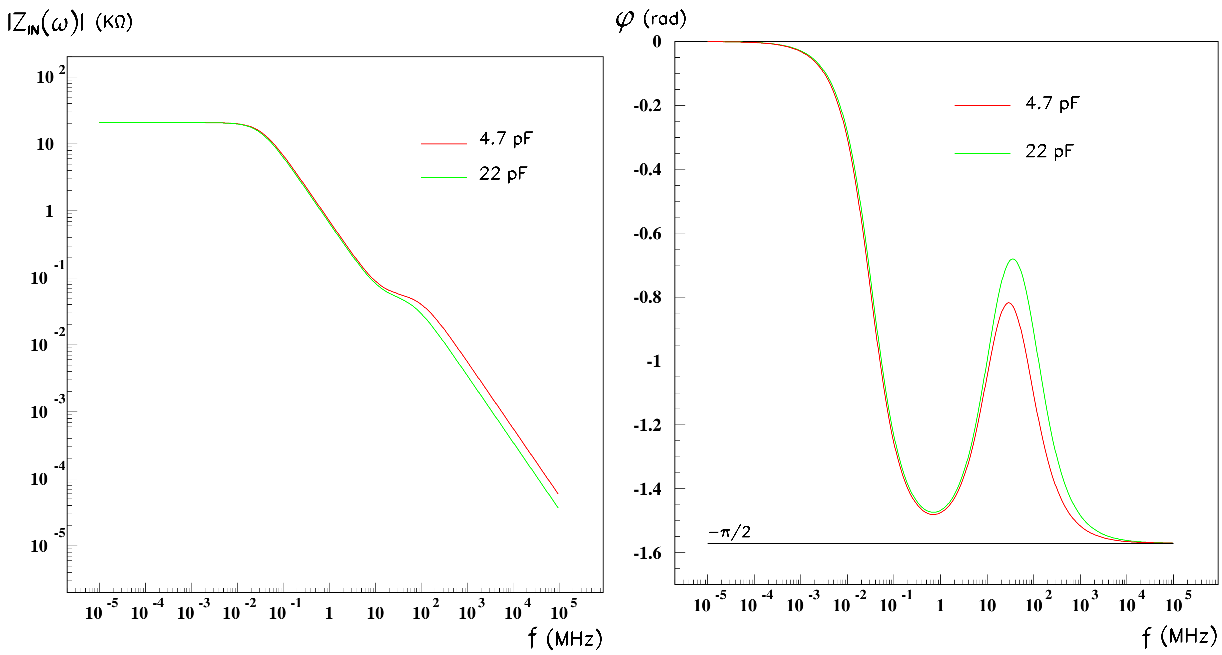

(a) (b)

Figure 15: Module (a) and phase (b) of APV25 input impedance.

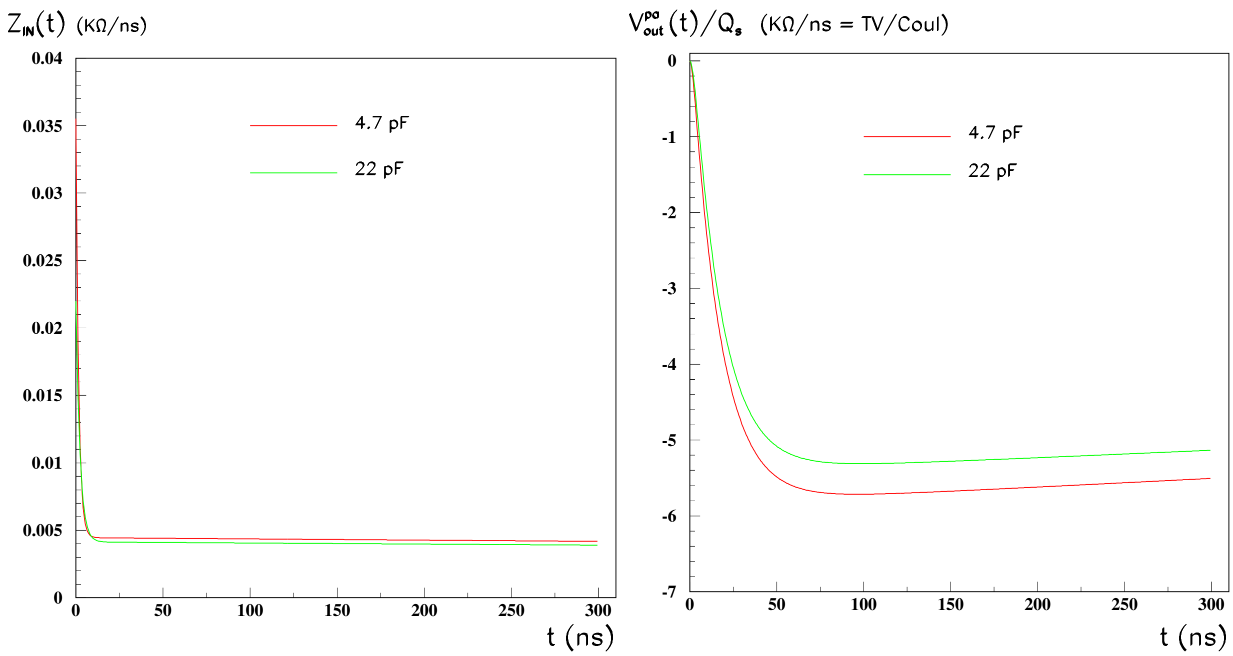

(a) (b)

Figure 16: Inverse Fourier transform of input impedance (a) and preamplifier output (b) for APV25.

6 Conclusions

We have reported about the parametrization of the CMS silicon detector front end output shape using two different models. The pulse shape analytical expressions allow to understand the influence of VSHA register on circuit performances by predictions on signal to noise ratio.

Moreover the even if approximative knowledge of circuit internal components has the advantage, in the still running experimentation, to give handles in order to reliably predict the behaviour of the front-end electronics in CMS future hard conditions of work.

Appendix

In this appendix the inverse Fourier transforms F(t) of transfer funcions $\tilde{F}(\omega)$ up to four poles, are listed.

Two poles

In case of two coincident real poles (CR-RC shaper):

$$\tilde{F}(\omega) = \frac{1}{(1+j\omega\tau)^2} \xrightarrow{\text{F.T.}} F(t) = \frac{t}{\tau^2} \cdot e^{-\frac{t}{\tau}} \tag{4}$$

In case of two distinct real poles τ_1 and τ_2:

$$\frac{1}{(1+j\omega\tau_1)(1+j\omega\tau_2)} \xrightarrow{\text{F.T.}} \frac{1}{\tau_1-\tau_2} \cdot \left(e^{-\frac{t}{\tau_1}} - e^{-\frac{t}{\tau_2}}\right) \tag{5}$$

In case of two complex poles θ and θ^*:

$$\frac{1}{(1+j\omega\theta)(1+j\omega\theta^*)} \xrightarrow{\text{F.T.}} \frac{t}{\tau_s^2\omega_0} \cdot e^{-\frac{t}{\tau_s}} \cdot \sin(\omega_0 t) \tag{6}$$

where:

$$\begin{cases} \tau_s &= \frac{|\theta|^2}{\Re(\theta)} \\ \omega_0 &= \frac{\Im(\theta)}{|\theta|^2} \end{cases}$$

Three poles

In the following all the different combination of three poles (real, complex coincident and not) transfer function transforms are reported:

$$\frac{1}{(1+j\omega\tau)^3} \xrightarrow{\text{F.T.}} \frac{1}{\tau^3} \cdot \frac{t^2}{2!} \cdot e^{-\frac{t}{\tau}} \tag{7}$$

$$\frac{1}{(1+j\omega\tau_1)(1+j\omega\tau_2)^2} \xrightarrow{\text{F.T.}} \frac{\tau_1}{(\tau_1-\tau_2)^2} \cdot \left[e^{-\frac{t}{\tau_1}} - \left(1 + \frac{\tau_1-\tau_2}{\tau_1\tau_2} \cdot t\right) \cdot e^{-\frac{t}{\tau_2}}\right] \tag{8}$$

$$\frac{1}{(1+j\omega\tau_1)(1+j\omega\tau_2)(1+j\omega\tau_3)} \xrightarrow{\text{F.T.}} A_1 \cdot e^{-\frac{t}{\tau_1}} + A_2 \cdot e^{-\frac{t}{\tau_2}} + A_3 \cdot e^{-\frac{t}{\tau_3}} \tag{9}$$

$$A_i = \frac{\tau_i}{(\tau_i-\tau_j)(\tau_i-\tau_k)} \qquad i,j,k = 1,2,3$$

$$\frac{1}{(1+j\omega\tau_r)(1+j\omega\theta)(1+j\omega\theta^*)} \xrightarrow{\text{F.T.}} A \cdot e^{-\frac{t}{\tau_r}} + (B \cdot \sin(\omega_0 t) + C \cdot \cos(\omega_0 t)) \cdot e^{-\frac{t}{\tau_s}} \tag{10}$$

where τ_s and ω_0 have been defined above, and:

$$\begin{cases} A &= \frac{\tau_r \cdot (1+\tau_s^2\omega_0^2)}{(\tau_s-\tau_r)^2+\omega_0^2\tau_r^2\tau_s^2} \\ B &= \frac{1+\tau_s^2\omega_0^2}{(\tau_s-\tau_r)^2+\omega_0^2\tau_r^2\tau_s^2} \cdot \frac{\tau_s-\tau_r}{\omega_0\tau_s} \\ C &= -\frac{\tau_r \cdot (1+\tau_s^2\omega_0^2)}{(\tau_s-\tau_r)^2+\omega_0^2\tau_r^2\tau_s^2} \end{cases}$$

Four poles

$$\frac{1}{(1+j\omega\tau)^4} \xrightarrow{\text{F.T.}} \frac{t^3}{\tau^4 \cdot 3!} \cdot e^{-\frac{t}{\tau}} \tag{11}$$

$$\frac{1}{(1+j\omega\tau_1)(1+j\omega\tau_2)^4} \xrightarrow{\text{F.T.}} \frac{\tau_1^3}{(\tau_1-\tau_2)^4} \cdot \left[e^{-\frac{t}{\tau_1}} - \sum_{k=0}^{3} \left(\frac{\tau_1-\tau_2}{\tau_1\tau_2} \cdot t \right)^k \frac{e^{-\frac{t}{\tau_2}}}{k!} \right] \tag{12}$$

$$\frac{1}{(1+j\omega\tau_1)(1+j\omega\tau_2)(1+j\omega\tau_3)^2} \xrightarrow{\text{F.T.}} A \cdot e^{-\frac{t}{\tau_1}} + B \cdot e^{-\frac{t}{\tau_2}} + (C + D \cdot t)\, e^{-\frac{t}{\tau_3}} \tag{13}$$

where:

$$\begin{cases} A &= \frac{\tau_1^2}{(\tau_1-\tau_2)(\tau_1-\tau_3)^2} \\ B &= \frac{\tau_2^2}{(\tau_2-\tau_1)(\tau_2-\tau_3)^2} \\ C &= \frac{1}{\tau_2-\tau_1} \cdot \left[\frac{\tau_1^2}{(\tau_1-\tau_3)^2} - \frac{\tau_2^2}{(\tau_2-\tau_3)^2} \right] \\ D &= \frac{1}{(\tau_3-\tau_1)(\tau_3-\tau_2)} \end{cases}$$

$$\frac{1}{(1+j\omega\tau_1)(1+j\omega\tau_2)(1+j\omega\tau_3)(1+j\omega\tau_4)} \xrightarrow{\text{F.T.}} A_1 \cdot e^{-\frac{t}{\tau_1}} + A_2 \cdot e^{-\frac{t}{\tau_2}} + A_3 \cdot e^{-\frac{t}{\tau_3}} + A_4 \cdot e^{-\frac{t}{\tau_4}}$$

$$A_i = \frac{\tau_i^2}{(\tau_i-\tau_j)(\tau_i-\tau_k)(\tau_i-\tau_l)} \qquad i,j,k,l = 1,2,3,4$$

$$\frac{1}{(1+j\omega\tau_{1r})(1+j\omega\tau_{2r})(1+j\omega\theta)(1+j\omega\theta^*)} \xrightarrow{\text{F.T.}} A \cdot e^{-\frac{t}{\tau_{1r}}} + B \cdot e^{-\frac{t}{\tau_{2r}}} + $$

$$+ \left(C \cdot \sin(\omega_0 t) + D \cdot \cos(\omega_0 t)\right) \cdot e^{-\frac{t}{\tau_s}} \tag{14}$$

where:

$$\begin{cases} A &= \frac{(1+\tau_s^2\omega_0^2)\tau_{1r}^2}{(\tau_{1r}-\tau_{2r})\cdot[(\tau_s-\tau_{1r})^2+(\omega_0\tau_s\tau_{1r})^2]} \\ B &= \frac{(1+\tau_s^2\omega_0^2)\tau_{2r}^2}{(\tau_{2r}-\tau_{1r})\cdot[(\tau_s-\tau_{2r})^2+(\omega_0\tau_s\tau_{2r})^2]} \\ C &= \frac{(1+\tau_s^2\omega_0^2)\cdot\left[\tau_{1r}\tau_{2r}(1-\tau_s^2\omega_0^2)+\tau_s(\tau_{1r}+\tau_{2r}-\tau_s)\right]}{\omega_0\cdot[(\tau_s-\tau_{1r})^2+(\omega_0\tau_s\tau_{1r})^2]\cdot[(\tau_s-\tau_{2r})^2+(\omega_0\tau_s\tau_{2r})^2]} \\ D &= \frac{(1+\tau_s^2\omega_0^2)\tau_s(2\tau_{1r}\tau_{2r}-\tau_{2r}\tau_s-\tau_{1r}\tau_s)}{[(\tau_s-\tau_{1r})^2+(\omega_0\tau_s\tau_{1r})^2]\cdot[(\tau_s-\tau_{2r})^2+(\omega_0\tau_s\tau_{2r})^2]} \end{cases}$$

References

[1] The APV6 Readout Chip for CMS Microstrips detectors, M. Raymond et al., Proceedings of Third Workshop on Electronics for LHC Experiments, CERN/LHCC/97-60,158-162.

[2] The APV25 deep submicron readout chip for CMS detectors, L.L. Jones et al., Fifth Workshop on Electronics for the LHC Experiments, Snowmass, Colorado, September 20-24, 1999.

[3] APV6 User Manual, M. French

[4] APV25 Test Results, M. Raymond, talk at CMS tracker week, 9/12/99.

[5] "Performance of the APV6 bonded to a full size Forward Milestone silicon detector", CMS note99_058, S. Busoni et al., INFN, Firenze, Italy.

[6] F. James, CERN Program Library Long Writeup D506 MINUIT, CERN, 1993